International Journal of Nanoelectronics and Materials
Volume 14, No. 2, April 2021 [179-194]

The Evolutions of Microstructure in Pressureless Sintered Silver Die Attach Material

S.R. Esa[1,4], G. Omar[1,2*], S.H. Sheikh Md Fadzullah[1], K.S Siow[3] and B. Abdul Rahim[4]

[1]Faculty of Mechanical Engineering, Universiti Teknikal Malaysia Melaka, Hang Tuah Jaya, 76100 Durian Tunggal, Melaka, Malaysia.
[2]Advanced Manufacturing Centre (AMC), Faculty of Mechanical Engineering, Universiti Teknikal Malaysia Melaka, Hang Tuah Jaya, 76100 Durian Tunggal, Melaka, Malaysia.
[3]Institute of Microengineering and Nanoelectronics, Universiti Kebangsaan Malaysia, 43600 Bangi, Selangor, Malaysia.
[4]MIMOS Semiconductor (M) Sdn. Bhd., Technology Park Malaysia, Bukit Jalil, 57000, Kuala Lumpur, Malaysia.

Received 8 March 2021, Revised 19 March 2021, Accepted 22 March 2021

ABSTRACT

Sintered silver (Ag) is one of the most promising interconnect materials for high temperature electronics applications due to its potential to withstand harsh and extreme environments. This paper investigates the microstructure evolutions of Ag particles under pressureless sintering in a polymeric adhesive binder at 200 °C, 250 °C, 275 °C, and 300 °C for a duration of 2 hours. The grains, particles, and neck growth observed via two-dimensional Focused Ion Beam (FIB) cuts on the samples at different sintering temperatures were associated with the atomic motions and reduction of surface energy that is the driving force for sintering. In this study, the pressureless sintering process in a polymeric adhesive binder successfully transformed the scattered Ag particles into a compact and dense Ag joining at 300 °C. The electrical conductivity value obtained at 300 °C was 5.2E+05 S/cm, which was the highest among the evaluation samples.

Keywords: Grain Size, Microstructure, Neck Growth, Porosity, Sintered Ag

1. INTRODUCTION

Lead containing solder alloys, such as tin-lead (SnPb) has dominated the interconnect technology for many decades [1-4]. Technological revolutions and ecological concerns have made the use of lead containing solder alloys as die attach materials no longer ideal [5,6]. Lead free solder alloys, such as tin-silver-copper (SAC), have then become an alternative to SnPb solder [7,8]. SAC solder alloys provide reasonable thermal performance (~60 W/mK), fast assembly, and low cost processing [9]. It also has broad compatibility with semiconductor packaging and surface mount technology (SMT) devices [10]. However, the use of lead-free solder alloys in high power semiconductor devices, such as wide band gap semiconductor and insulated-gate bipolar transistor (IGBT), possess several shortcomings due to high working temperatures. These temperatures are well above the melting point of solder and can cause the solder joining to deteriorate [11]. The coefficient of thermal expansion (CTE) mismatch due to different material properties in the interconnect systems can lead to interface stress and critical reliability issues [12]. Additionally, uncontrollable intermetallic compounds (IMCs) growth after soldering process induces another metallurgical-joint issue that leads to reliability degradation [13,14].

* Corresponding Author: ghazali@utem.edu.my

The emergence of sintered Ag die attached material is motivated by the requirement in developing a new material that can overcome the limitation of solder material and can cope with high operating temperatures [15,16]. The prospect of sintered Ag material that can withstand harsh and extreme environments has made it to be in great demand [17]. The importance of sintered Ag material is also reflected by a substantial increase in the published research papers and patents filed related to sintered Ag as a workable technology [18-21]. Sintered Ag materials are typically composed of micron, sub-micron, and/or nano particles that can be diffused in the temperature range of 180 °C to 300 °C [22]. The diffusion mechanism is initiated by atomic diffusions among Ag particles and subsequently forming a microporous joining [23]. The microporous sintered Ag joining has a melting point of 961 °C, which is similar to the melting point of bulk Ag material, thus Ag sinter joining can be used in high temperature applications exceeding 300 °C [24]. Sintered Ag offers high reliability performance and high thermal conductivity of 200-300 W/mK, about three times greater than solder die attach materials [25,26]. In sintered Ag die attach material, the intermetallic bonds between Ag particles determines the heat conduction path.

It is important to have a fundamental understanding of the properties and behaviours of Ag during sintering in order to obtain the desired interconnect characteristic for die attach process. Ag sintering behaviour depends on materials and process variables that can influence the sinterability and microstructure of the sintered materials [27]. Typically, material variables are related to the raw material properties such as particle shape, particle size, grain size, composition, and green density. On the other hand, process variables are related to the sintering conditions, such as temperature, time, atmosphere, pressure, and heating rate [28,29]. High pressure sintering has been introduced in the early stages of sintered Ag development to assist the bonding process since Ag particles were in micron sizes. Ag pressure sintering results in high reliability, as it can eliminate residual porosity without excessive grain growth [30]. However, Ag pressure sintering may induce fracture or damage to the IC devices. It is also an expensive process and has a very low manufacturing output. Hence, it is important to explore the characteristic of Ag under pressureless condition to overcome the limitation in pressure sintering condition.

Most of the previous studies were based on pure sintered Ag joint [31,32]. However, in this study, a polymeric adhesive binder was pre-mixed with sub-micron Ag particles for pressureless sintering in air to understand the microstructural evolutions. This paper includes in-depth characterization of sintered Ag joint, such as particle shape transformations, grain size, particle size, neck growth, density, and pore formations. The electrical conductivity was measured to correlate the microstructure change to the conductivity improvement of sintered Ag. The findings can be useful for certain niche applications, especially for high power electronics application.

2. EXPERIMENTAL DETAILS

Ag paste material used in this study consisted of spherical Ag particles with an average particle size of 420 nm. The paste constituents are 80% Ag and 20% binder made up of 12% polymeric material and 8% solvent. The Ag paste was printed manually onto 1.5 cm x 1.5 cm silicon (Si) substrate as illustrated in Figure 1. The Si substrate was only used as a sample carrier or base material for the sintering process. It was expected that no interaction occurs between the Ag paste material and the Si substrate. Furthermore, this study is focusing mainly on the Ag paste material and not on the interaction between Ag paste materials to the substrate used. Four groups of samples were prepared and were subjected to a pressureless sintering process in air using a thermal oven at 200 °C, 250 °C, 275 °C, and 300 °C, for a duration of 2 hours.

Figure 1. The as-received Ag paste sample.

The microstructure variations at different sintering temperatures were investigated by means of Focused Ion Beam (FIB) micro sectioning. The FIB system used in this study was the FEI Helios Nanolab 650 that has both ion milling and electron microscopy capability. The FIB system uses a 30 kV gallium (Ga^+) ion beam with fast and precise milling that enables inspection at the cross-sectional view of the sample. The microstructure observation was carried out using secondary electron microscopy with an imaging resolution of 1 nm and acceleration voltage of 2 kV. The detailed microstructure observations were performed on each evaluation sample by observing the changes in particle size, grain size, neck growth, and pore formations after sintering process.

A 200 kV FEI Tecnai G^2 F20 X-Twin High Resolution Transmission Electron Microscopy (HRTEM) system with 0.2 nm resolution was employed to observe the atomic structure of Ag paste material. The lamella was prepared by *in-situ lift out* technique using FIB equipment and was attached onto a copper (Cu) grid finger. It was then thinned down to an electron transparency, which was less than 100 nm prior to HRTEM inspection.

The quantitative analysis of the porosity and pore size of the sintered Ag samples was performed automatically by using image J software. The electron micrographs of the sintered Ag samples were converted into binary images for calculation. In order to quantify the neck growth at different sintering temperatures, the neck width between two connecting Ag particles was measured as illustrated in Figure 2. The neck width is defined as a diameter of the sinter bond between two particles. According to a theoretical model developed by Kuczynski, the neck growth can be calculated using the following equation [33,34]:

$$\left(\frac{X}{D}\right)^n \sim t \tag{1}$$

where D is the particle diameter, X is the neck width, t is the sintering time, and n is the predicted model depending on the diffusion form.

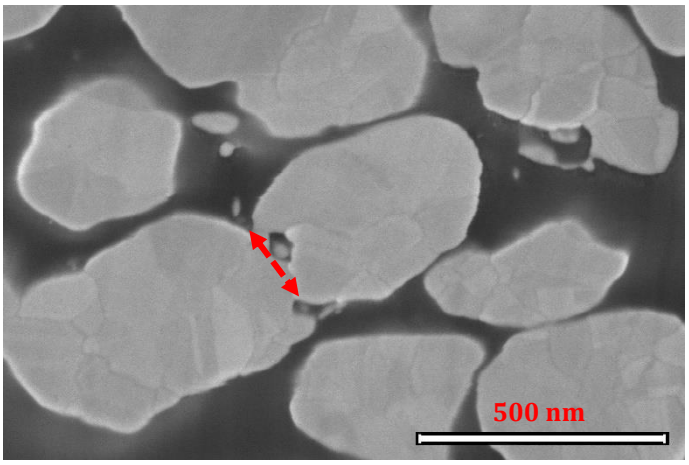

Figure 2. The measurement of neck width between two connecting particles.

The conductivity and resistivity of the as-received Ag paste sample and after sintering were measured using Ecopia HMS-5300 Hall Effect instrument as shown in Figure 3. The system consists of four point probes that contact directly with the sample surface during measurement. The conductivity and resistivity measurements were conducted automatically using Ecopia HMS-5300 V5.8.0.7 software.

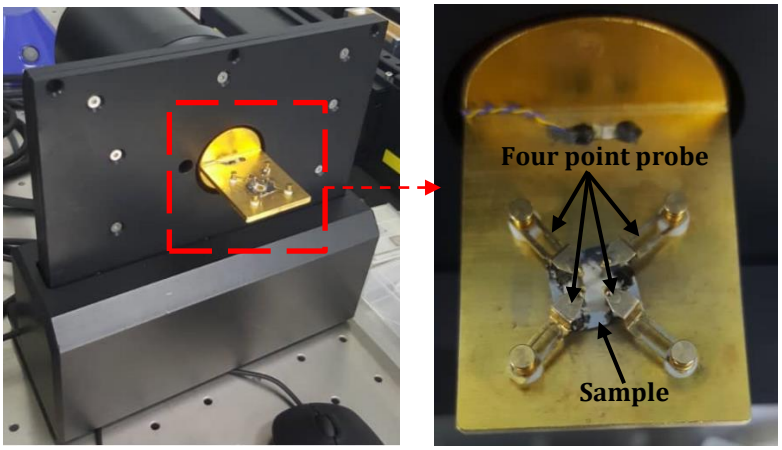

Figure 3. The four point probes of Hall Effect system.

3. RESULTS AND DISCUSSION

3.1 Ag particles necking formation and grain growth

Figure 4 shows the FIB micrographs of the samples that were subjected to the sintering process of 200 °C, 250 °C, 275 °C, and 300 °C for 2 hours. The presence of nearly spherical shaped Ag particles was observed on sample sintered at 200 °C. Some of the particles were found to be in intimate contact with each other, but some particles were scattered with no contact. At thermal energy of 250 °C, the appearance of nearly spherical shaped Ag particles were still visible. However, the neck formations between the particles were seen to be connecting them into a three-dimensional network. The Ag particles then transformed into elongated and irregular shapes at 275 °C. Grain size enlargement was also visible. The increase of thermal energy to 300 °C completely transformed the Ag particles into a solid Ag structure. Qualitatively, it was also observed that some of the grains of the sample at 300 °C sintering temperature was much larger than the particle size of sample sintered at 200 °C. The densification and grain growth dominated the microstructural evolution at 300 °C.

The phenomenon of necking formations and the transformation of Ag particles from individual particles into a solid structure at higher thermal energy are the results from sintering process [35]. This demonstrates that thermal energy is an important process variable in sintering. The extrinsic energy supply can thermally activate and initiate the particles to form inter-particle bonds through necking between them [36]. Theoretically, energy exists on the particle surface due to atoms not being fully bonded, unlike the bulk properties of the particles, where the atoms are generally stable and have a balanced set of bonds. Therefore, the particle surface has much higher energy than those in the bulk region [37]. When two or more particles are in mutual contact, they are not in a thermodynamically equilibrium state due to excess surface energy. Consequently, bonding between particles takes place over a period of time, resulting in a reduction of total surface area and releasing of surface energy. In addition, the application of thermal energy will enhance and speed up this bonding process. From a thermodynamic

perspective, the sintering process is driven by the reduction of energy on the particle surface, promoting the atomic diffusion between the particles [38]. The thermal energy that was introduced during sintering process stimulates the atomic motion that allows sintering to proceed. Sintering process is faster at higher temperatures, due to the increased in the number of active atoms and available sites. The Arrhenius relation describes that the probability for an atom to have enough energy to move is determined by the activation energy, Q. The volume diffusion coefficient, D_V is determined from the atomic vibrational frequency D_0, absolute temperature, T, universal gas constant, R, and the activation energy, Q, which corresponds to the energy required to induce atomic diffusion via vacancy exchange according to the following equation [39];

$$D_V = D_0 \, exp \, (-\frac{Q}{RT}) \tag{2}$$

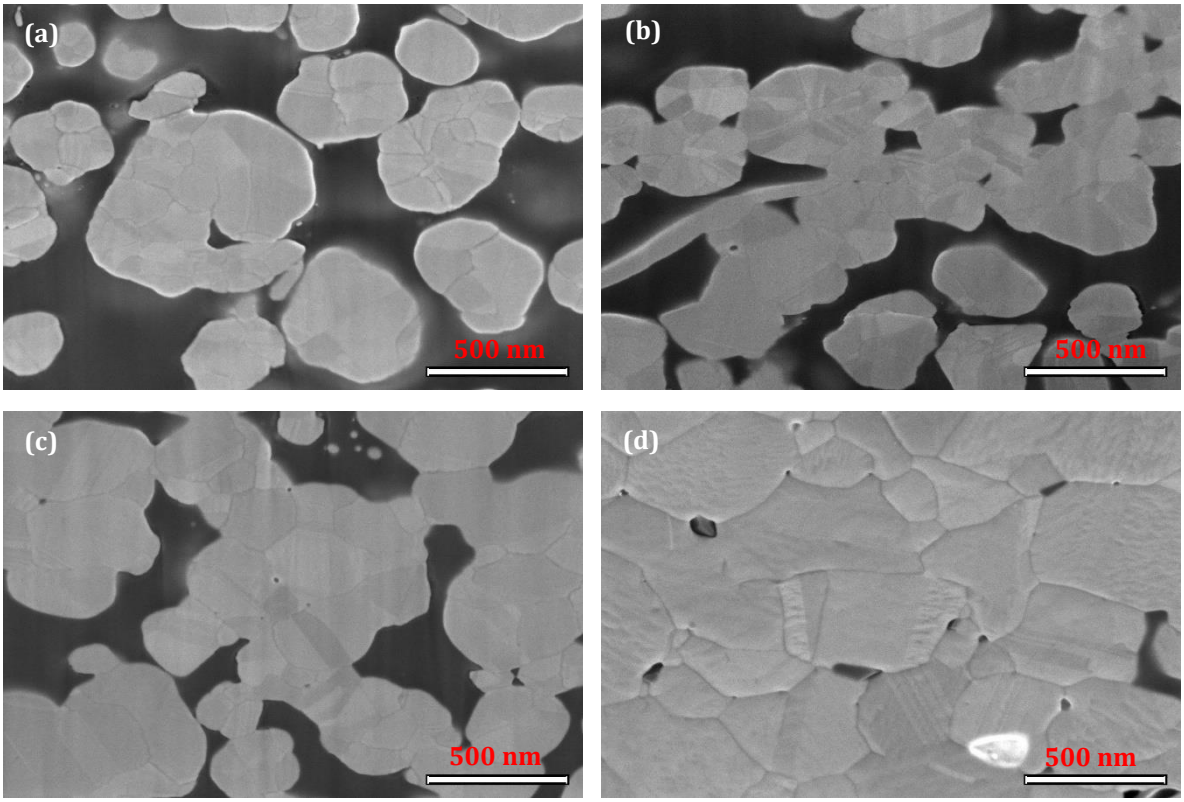

Figure 4. FIB micrographs for sample at 200 °C, 250 °C, 275 °C, and 300 °C sintering temperature.

Figure 5 shows the plot of quantitative measurement results for particle and grain size of the samples at different sintering temperature. In average, the particle and grain size tend to increase with increasing thermal energy. The average particle sizes were 442 nm, 506 nm, and 913 nm for 200 °C, 250 °C, and 275 °C sintering temperature, respectively, while the corresponding average grain sizes were 149 nm, 155 nm, 207 nm, and 460 nm. The maximum grain size at 300 °C was 1533 nm, which was 29 % larger than the average particle size at 200 °C. In general, it can be deduced from the graph that the particle size growth rate was much higher than that of grain size growth rate. Additionally, the rate of grain size growth was lower at 200 °C and increased at 300 °C. The most significant variation of particle size can be observed in the sample sintered at 275 °C, where the particle sizes ranged from 445 nm to 1626 nm. On the other hand, the sample at sintered 300 °C showed the most significant variation of grain size, ranging from 136 nm to 1533 nm.

Sample sintered at 300 °C transformed from individual particles into a solid metal structure due to the densification and grain coarsening effects resulted from the sintering process. Therefore, no isolated particle size data was obtained from this sample. The densification effect was due to the change in surface energy, ΔY, where the interface between Ag particles diminished and led to the formation of Ag to Ag joining. The region between the particles that was previously occupied by the polymeric binders diminished during this stage due to evaporation of the polymers. The grain coarsening occurred due to the change in surface area, ΔA, where the grain growth resulted in bigger grains and solid metal formations. Therefore, the reduction of total energy, $\Delta(YA)$ on the surface atoms can be determined by the following equation [40];

$$\Delta(YA) = (\Delta Y)A + Y(\Delta A) \tag{3}$$

The total surface energy, YA, determines the strength of the driving force for sintering, which is inversely proportional to the particle diameter. The initial total surface area, A, determines the rate of sintering. In general, a smaller initial particle size facilitates better sintering due to larger surface area, higher energy per unit volume, and higher curvature as compared with a bigger particle size. Simply put, smaller particles would diffuse faster at lower energy that the larger ones. These characteristics enhance the sintering process. Given an amount of material with volume, V_0, the total surface area, A, increases with a reduction of particle size, d, according to the following equation [41]:

$$A = \frac{6V_0}{d} \tag{4}$$

The diffusion transport and mechanism are enhanced with larger surface area through surface diffusion, while smaller grain size promotes the grain boundary diffusion and larger inter-particle contact area to volume diffusions [42].

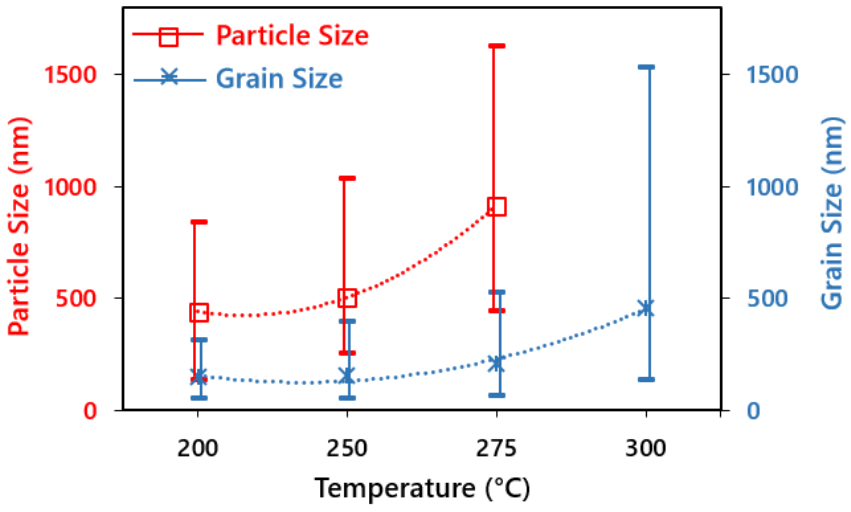

Figure 5. The average particle size and grain size at different sintering temperature.

Figure 6 shows the average neck width taken from 30 measurements on samples sintered at 200 °C, 250 °C, and 275 °C. In average, the neck width increases as the sintering temperature increases. The average neck width was 138 nm, 204 nm, and 313 nm for sintering temperature 200 °C, 250 °C, and 275 °C, respectively. The neck width of sample sintered at 275 °C was 2.3

times higher than the sample sintered at 200 °C. The most significant variation of neck width was observed for sample sintered at 275 °C, where the neck width ranged from 159 nm to 571 nm. The neck growth ratio was measured by taking the ratio between the width of the neck and the neighbouring particle diameter. The average neck growth ratio was 0.36, 0.45, and 0.63 for 200 °C, 250 °C, and 275 °C, respectively as shown in Figure 6. The largest necking growth ratio for sample sintered at 275 °C was 0.86.

The neck formations initiated at the contact points between two adjacent particles. Particle size also plays an important role in neck growth. This is because neck formations and growth are associated with the reduction of surface energy that is the driving force for sintering [43]. Some of the energy is also used to balance the simultaneous grain boundary formations. Thus, neck growth also increasing the grain boundary area through grain boundary diffusions. The neck growth progresses until surface energy and grain boundary energy attains an equilibrium state. At this point, the neck growth and grain growth generally increase over time, which is typically enhanced and speeded up by external thermal energy sources [44]. In a previous study by Chen, high surface energy on the Ag particle surface not only facilitated the sintering process in terms of neck formation and growth, but also contributed to the formation of robust and reliable bonding between the sintered Ag and its substrate [45].

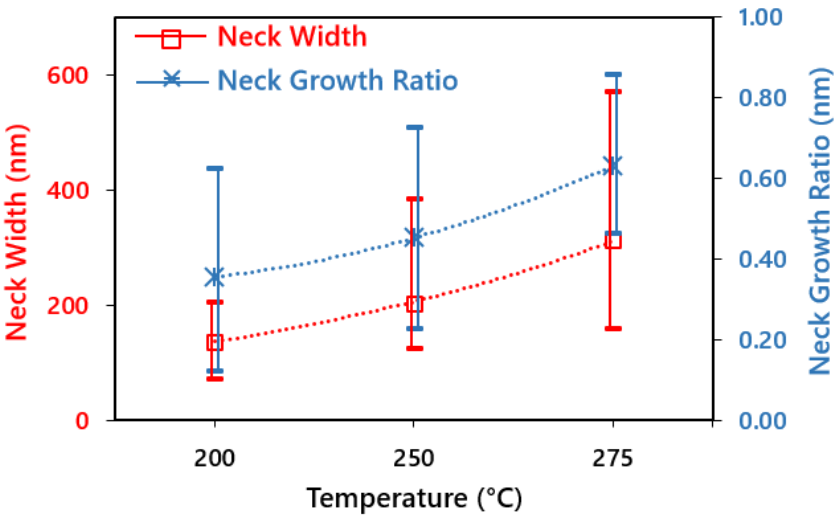

Figure 6. The average neck width and neck growth ratio at different sintering temperature.

Figure 7 shows the HRTEM image of Ag particles. It can be clearly observed that Ag particle is a polycrystalline material with multiple grain structures. Each grain structure has its own crystallographic orientation and is separated by a grain boundary. There are large amounts of vacant sites that exist along the grain boundary due to the atoms not being tightly bonded to the adjacent atoms than those at the inner positions. Thus, atoms in the grain boundary area have higher energy states than those in the inner positions. This energy is called as interfacial energy or grain boundary energy, and the magnitude of this energy is a function of the degree of the crystallographic misalignment. High energy states that exist at the grain boundary promote grain boundary diffusion during neck growth and thereby induces grain growth. Grain growth is a microstructural evolution due to grain boundary diffusion. The resulting grain growth means there is an increase in average grain sizes and a decrease in the number of grains. Figure 8 shows the plot of grain number at different sintering temperatures. The number of grains was 172 at 200 °C and reduced to 56 at 300 °C as shown in the graph. The driving force for grain growth was

the reduction in interfacial energy associated with the grain boundary diffusion in order to minimize the total energy of the systems [46].

The degree of crystallinity was also found to influence the bonding quality of sintered Ag. Different conditions during synthesis of Ag particles may lead to differences in the degree of lattice expansion and contraction, thus producing a different level of crystallinity. Paknejad, in his study, observed that high degree of crystallinity leads to high thermal conductivity, high die shear strength, and improved joining strength during sintering [47].

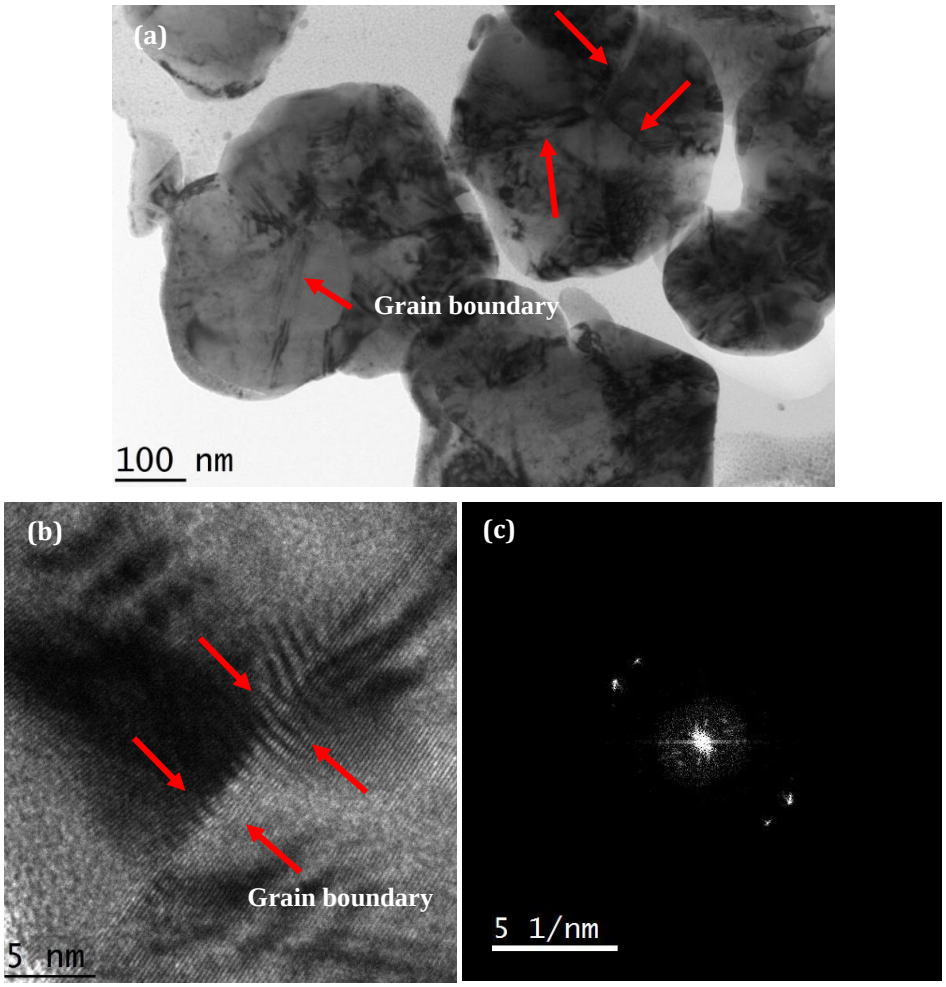

Figure 7. HRTEM micrograph of polycyrstalline Ag particle. (a) TEM image, (b) HRTEM image shows the grain boundary and (c) the corresponding FFT pattern.

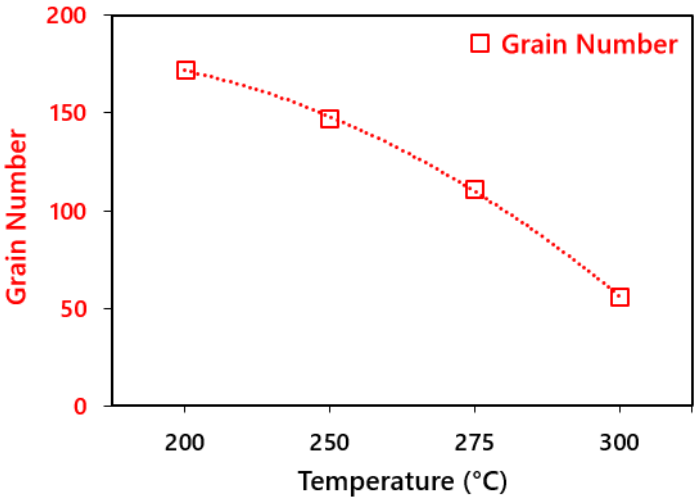

Figure 8. Grain number at different sintering temperature.

3.2 Pore Formation

The porosity and average pore size were calculated automatically by converting the FIB cross sectioned image into a binary image by using image J software as shown in Figure 9. In the converted image, sintered Ag and pore areas were transformed into black and white, respectively as shown in Figure 9(a). The red outline in Figure 9(b) and (c) represent the boundary of pore areas. Image J calculated both porosity and pore size automatically according to the defined red outline. The average area of the pore was used as the pore size.

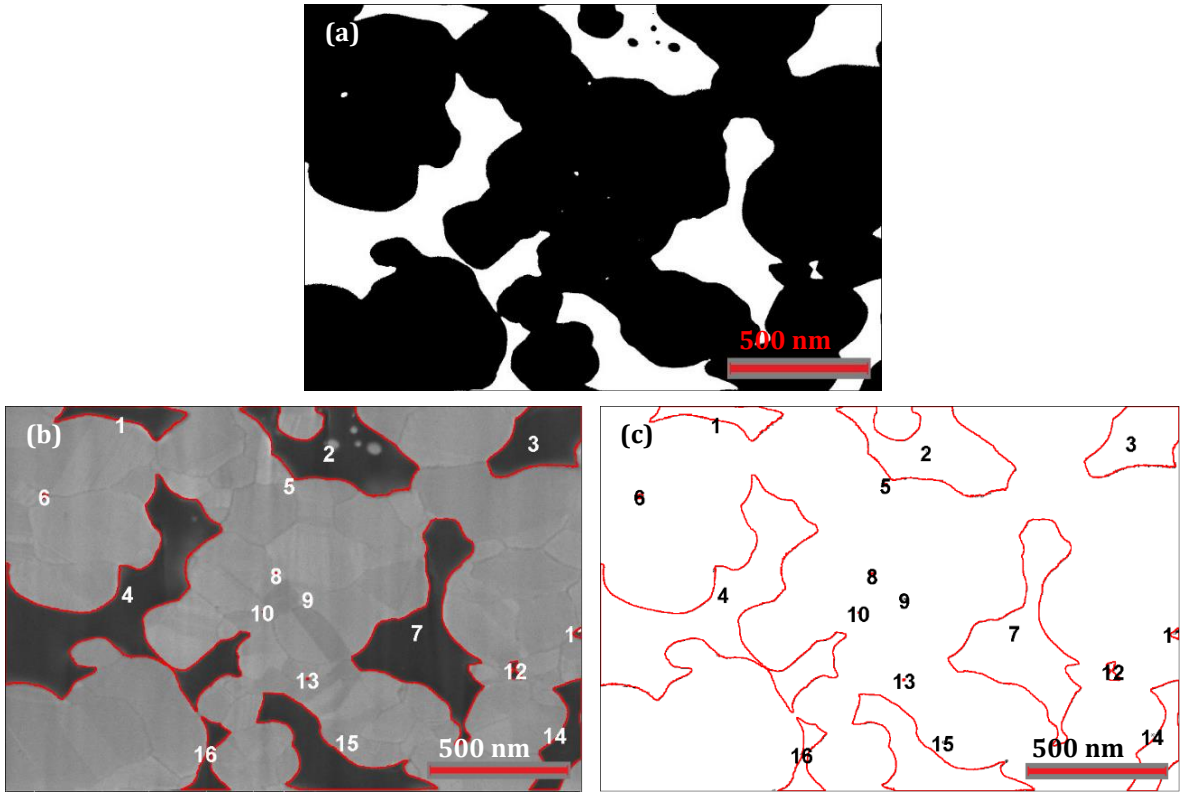

Figure 9. The corresponding binary image and automated pore size calculation using Image J.

Figure 10 shows the porosity and average pore size as calculated using Image J software. The porosity of Ag sintered at 200 °C, 250 °C, 275 °C, and 300 °C was 43%, 35%, 18%, and 2%, while the average pore size was 1496 nm, 628 nm, 308 nm, and 118 nm, respectively. The sample sintered at 200 °C was found to have the highest porosity level, while a significant reduction of porosity was observed for sample sintered at 300 °C.

At 200 °C, the sample exhibited signs of early stage sintering, where the pore area was relatively large due to less contact between the Ag particles. At this stage, the inter-particle contact was initiated through smaller particle size, as small particle has a larger surface area to volume ratio, causing lower thermal energy to be enough for the particle to diffuse. The characteristic of the intermediate sintering stage was observed in the sample sintered at 275 °C, where further increases of particle contact reduced the pore area giving a density of 82%. At even higher temperature of 300 °C, the dewetting and evaporation of the polymer binder caused the particles to become closer to each other, yielding to the close contact of the particles. This temperature range also provided enough thermal energy for bigger particles to diffuse. With a continuous supply of thermal energy, the pore size reduced, especially at the triple junction through the densification and grain growth. As a result, the final stage of sintering obtained a density of sintered Ag reaching 98%. Based on this observation, it can be deduced that from intermediate to the final stage, the decrease in pore size indicates that the densification dominated the process.

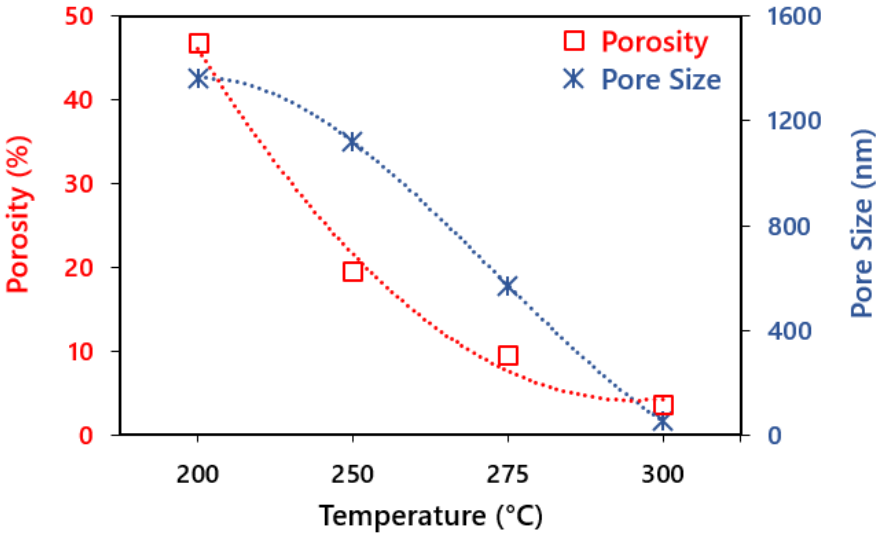

Figure 10. The porosity and pore size after exposure at different sintering temperature.

Polycrystalline Ag particles contain multiple grain structures resulting in multiple grain boundaries. At the final stage of sintering, pores are entrapped mostly at the grain boundaries, especially at the triple junctions. This microstructure suggests that pores migrate along the grain boundaries during the particles joining and grain growth [48]. Porosity reduction is associated with the mechanism of grain growth, in which it acts as a driving force to reduce the surface energy [49].

The pore size and formation are dependent on the particle size and shape. A variation in particle size and shape may also result in non-uniform pore formation. The grain growth at the initial stage of sintering could also affect the pore formation during the final stage of sintering [50]. In order to explain the mechanism of pore formation, a sintering model of particle is used as illustrated in Figure 11. At the initial stage of sintering, Ag particle came into intimate contact and necks were formed between the particles. Further increase of contact area during the

intermediate stage formed an interconnect pore, especially along the grain boundary regions. As the sintering process continued, the interconnect pore was discontinued and formed isolated pores. At the same time, the grains continued to grow. This stage is known as the final stage of sintering.

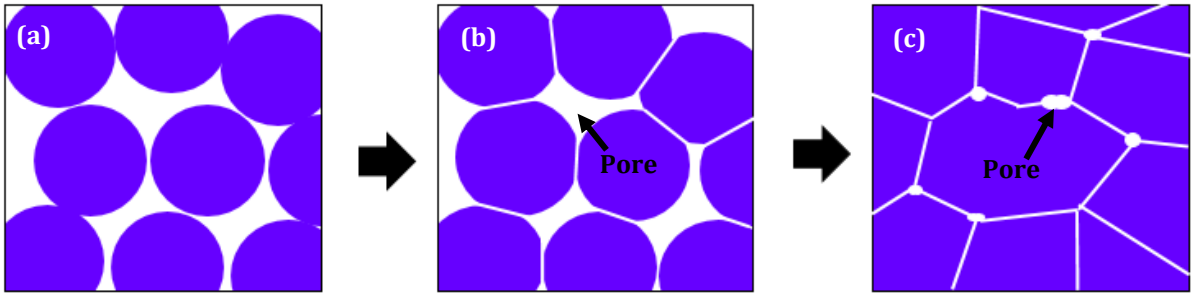

Figure 11. The mechanism of pore formation.

3.3 Conductivity

In order to correlate the microstructure with conductivity improvement, each of the samples were subjected to conductivity and resistivity measurements using a hall effect instrument. Figure 12 shows the results of conductivity and resistivity for samples at RT, 100 °C, 200 °C, 250 °C, 275 °C, and 300 °C sintering temperatures. Sample at RT, that was not subjected to external thermal energy, had an average resistivity value of 2.5E-01 Ohm cm, which was the highest among other samples. On the other hand, it showed an increasing trend in conductivity as the thermal energy increases. Sample sintered at 275 °C showed an average conductivity value of 2.6E+05 S/cm, while sample that was subjected to 300 °C thermal energy showed an average conductivity value of 5.2E+05 S/cm, which was the highest among other samples.

The improvement in conductivity and the reduction in resistivity was associated with the inter-particles joining and networking between the Ag particles. Sample sintered at 300 °C showed the highest Ag density and compactness, thus giving higher conductivity value. Moreover, the reduction in porosity was found to have an effect in increasing the conductivity of the sintered Ag sample [51].

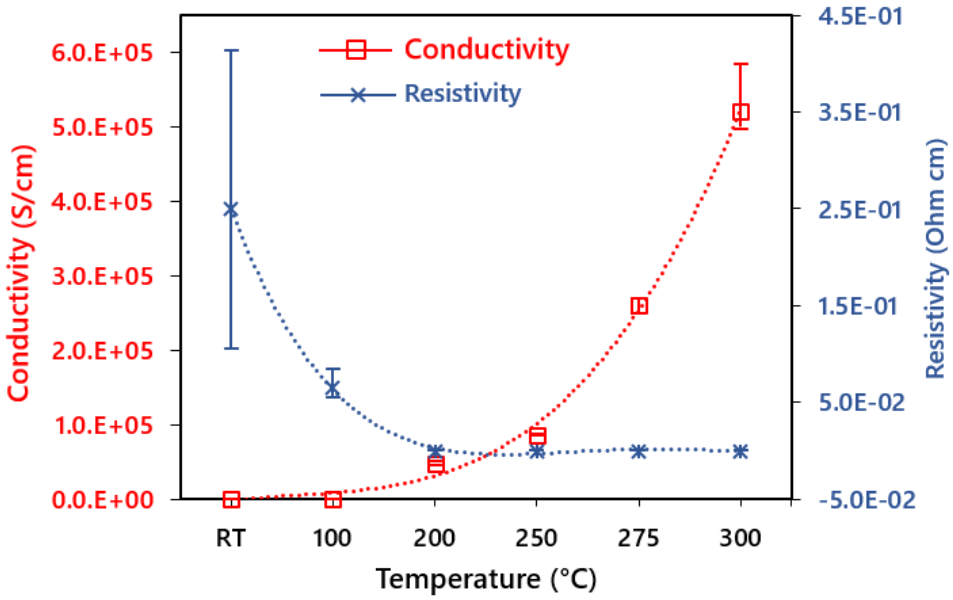

Figure 12. The conductivity and resistivity of sintered Ag at different sintering temperature.

4. CONCLUSION

The microstructure evolution was observed in sintered Ag samples as they make intimate contact and further neck growth during the intermediate stage of sintering. The neck formations and growth were associated with the reduction of surface energy that is the driving force for sintering. Additionally, the neck growth and grain growth reduced the pore area and improved the density of the sinter joints. In this study, the pressureless sintering process successfully formed a compact and dense Ag joining at 300 °C. The improvement in conductivity was observed at 300 °C, giving the value of 5.2E+05 S/cm, which was the highest among other evaluation samples.

ACKNOWLEDGEMENTS

The authors are gratefully acknowledging the Advanced Manufacturing Centre (AMC), Lab Research Advanced Materials Characterization Laboratory (AMCHAL), the financial support from Universiti Teknikal Malaysia Melaka, Ministry of Education, Malaysia under FRGS Grant, Project no. FRGS/2018/FKM/ F0366. The authors also would like to acknowledge Dr Shutesh Krishnan from ON Semiconductor (M) Sdn. Bhd. for his help in this publication.

REFERENCES

[1] Shualdi, W., Bais, B., Ahmad, I., Omar, G. and Isnin, A., "Nanoindentation Characterization of Sn-Ag-Sb/Cu Substrate IMC Layer Subject to Thermal Aging," In IEEE Regional Symposium on Micro and Nano Electronics, (2011) pp. 220-223.

[2] Xu, J., Wu, M., Pu, J. and Xue, S., "Novel Au-Based Solder Alloys: A Potential Answer for Electrical Packaging Problem," Advances in Materials Science and Engineering, (2020).

[3] Amares, S., and D. Rajkumar., "Environmental Friendly Low Mass 20g-Sn58Bi/Cu Solder Alloy as an Alternative to Lead SnPb and Its Properties Study," In IOP Conference Series: Earth and Environmental Science, vol. **505**, no. 1, (2020) p. 012004.

[4] Ghaleeh, M., Baroutaji, A. and Al Qubeissi, M., "Microstructure, Isothermal and Thermomechanical Fatigue Behaviour of Leaded and Lead-Free Solder Joints," Engineering Failure Analysis, vol. **117**, (2020) p. 104846.

[5] Cruz, C., Lima, T., Soares, M., Freitas, E., Fujiwara, E., Garcia, A. and Cheung, N., "Effect of Microstructure Features on the Corrosion Behavior of the Sn-2.1 wt% Mg Solder Alloy," Electronic Materials Letters, (2020) pp. 1-17.

[6] Yunos, A.M., Omar, G. and Masripan, N.A.B., "The Effect of Different Shape Pattern of Metal Interconnects on the Electrical and Mechanical Properties of Stretchable Conductive Circuit," Journal of Mechanical Engineering and Technology, vol. **11**, no. 1, (2019) pp. 22-29.

[7] Cheng, S., Huang, C.M. and Pecht, M., "A Review of Lead-Free Solders for Electronics Applications," Microelectronics Reliability, vol. **75**, (2017) pp. 77-95.

[8] Zhang, P., Xue, S. and Wang, J., "New Challenges of Miniaturization of Electronic Devices: Electromigration and Thermomigration in Lead-Free Solder Joints," Materials and Design, vol. **192**, (2020) p. 108726.

[9] Chen, C.J., Chen, C.M., Horng, R.H., Wuu, D.S. and Hong, J.S., "Thermal Management and Interfacial Properties in High-power GaN-based Light-Emitting Diodes Employing Diamond-Added Sn-3 wt.% Ag-0.5 wt.% Cu Solder as a Die-Attach Material," Journal of Electronic Materials, vol. **39**, no. 12, (2010) pp. 2618-2626.

[10] Ani, F.C., Jalar, A., Saad, A.A., Khor, C.Y., Abas, M.A., Bachok, Z. and Othman, N.K., "Characterization of SAC–x NiO Nano-Reinforced Lead-Free Solder Joint in an Ultra-Fine Package Assembly," Soldering & Surface Mount Technology, vol. **31**, no. 2, (2019) pp. 109-124.

[11] Zhang, H., Zhu, Q.S., Liu, Z.Q., Zhang, L., Guo, H. and Lai, C.M., "Effect of Fe Content on the Interfacial Reliability of SnAgCu/Fe-Ni Solder Joints," Journal of Material Science and Technology, vol. **30**, no. 9, (2014) pp. 928-933.

[12] Wang, J., Niu, Y. and Park, S., "An Investigation of Moisture-Induced Interfacial Delamination in Plastic IC Package during Solder Reflow," In International Electronic Packaging Technical Conference and Exhibition, American Society of Mechanical Engineers, vol. **58097**, (2017) p. V001T01A011.

[13] Shualdi, W., Ahmad, I., Omar, G. and Isnin, A., "Intermetallic Growth of Sn-Ag-Sb/Ni Plated Cu in Power Packaging Subject to Thermal Aging," In 33rd IEEE/CPMT International Electronics Manufacturing Technology Conference, (2008) pp. 1-5.

[14] Li, Z.L., Cheng, L.X., Li, G.Y., Huang, J.H. and Tang, Y., "Effects of Joint Size and Isothermal Aging on Interfacial IMC Growth in Sn-3.0 Ag-0.5 Cu-0.1 TiO2 Solder Joints," Journal of Alloys and Compounds, vol. **697**, (2017) pp. 104-113.

[15] Qian, C., Gheitaghy, A.M., Fan, J., Tang, H., Sun, B., Ye, H. and Zhang, G., "Thermal Management on IGBT Power Electronic Devices and Modules," IEEE Access, vol. **6**, (2018) pp. 12868-12884.

[16] Zhang, H., Li, W., Gao, Y., Jiu, J. and Suganuma, K., "Enhancing Low-temperature and Pressureless Sintering of Micron Silver Paste based on an Ether-type Solvent," Journal of Electronic Materials, vol. **46**, no. 8, (2017) pp. 5201-5208.

[17] Tan, Y.S., Li, X., Chen, X., Lu, G.Q. and Mei, Y.H., "Low-Pressure-Assisted Large-Area (> 800 mm2) Sintered-Silver Bonding for High-Power Electronic Packaging," In IEEE Transactions

on Components, Packaging and Manufacturing Technology, vol. **8**, no. 2, (2017) pp. 202-209.

[18] Fukushima, H., & Hanya, A., "Composition for Sintering, Method for Producing Silver Nanoparticles, Circuit Board, and Method for Manufacturing Circuit Board," U.S. Patent No. 10,774,231. Washington, DC: U.S. Patent and Trademark Office, (2020).

[19] Siow, K. S., and Y. T. Lin., "Identifying the Development State of Sintered Silver (Ag) as a Bonding Material in the Microelectronic Packaging via a Patent Landscape Study," Journal of Electronic Packaging , vol. **138,** no. 2, (2016) pp. 1–18.

[20] Yunos, A.M., Omar, G., Salim, M.A., Masripan, N.A. and Al-Mola, M.H.A., "The Effect of Temperature on the Electrical Conductivity and Microstructure Behaviour of Silver Particles," International Journal of Nanoelectronics and Materials, vol. **13**, (2020) pp. 431-438.

[21] Esa, S.R., Omar, G., Fadzullah, S.H., Siow, K.S., Rahim, B.A. and Çoşut, B., "Diffusion Mechanism of Silver Particles in Polymer Binder for Die Attach Interconnect Technology," International Journal of Nanoelectronics and Materials, vol. **13**, (2020) pp. 461-472.

[22] Zhang, Z., Chen, C., Yang, Y., Zhang, H., Kim, D., Sugahara, T., Nagao, S. and Suganuma, K., "Low-Temperature and Pressureless Sinter Joining of Cu with Micron/Submicron Ag Particle Paste in Air," Journal of Alloys and Compounds, vol. **780**, (2019) pp. 435-442.

[23] Gadaud, P., Caccuri, V., Bertheau, D., Carr, J. and Milhet, X., "Ageing Sintered Silver: Relationship between Tensile Behavior, Mechanical Properties and the Nanoporous Structure Evolution," Materials Science and Engineering: A, vol. **669**, (2016) pp. 379-386.

[24] Riva, R., Buttay, C., Allard, B. and Bevilacqua, P., "Migration Issues in Sintered-Silver Die Attaches Operating at High Temperature," Microelectronics Reliability, vol. **53**, no. 9-11, (2013) pp. 1592-1596.

[25] Chen, C. and Suganuma, K., "Microstructure and Mechanical Properties of Sintered Ag Particles with Flake and Spherical Shape from Nano to Micro Size," Materials and Design, vol. **162**, (2019) pp. 311-321.

[26] Bai, J.G. and Lu, G.Q., "Thermomechanical Reliability of Low-Temperature Sintered Silver Die Attached SiC Power Device Assembly," In IEEE Transactions on Device and Materials Reliability, vol. **6**, no. 3, (2006) pp. 436-441.

[27] Norazman, F. and Hopkinson, N., "Effect of Sintering Parameters and Flow Agent on the Mechanical Properties of High Speed Sintered Elastomer," Journal of Manufacturing Science and Engineering, vol. **136**, no. 6, (2014) pp. 1-7.

[28] Siow, K.S., "Mechanical Properties of Nano-Silver Joints as Die Attach Materials," Journal of Alloys and Compounds, vol. **514**, (2012) pp. 6-19.

[29] Siow, K.S., "Are Sintered Silver Joints Ready for use as Interconnect Material in Microelectronic Packaging?," Journal of Electronic Materials, vol. **43**, no. 4, (2014) pp. 947-961.

[30] Liu, Y., Zhang, H., Wang, L., Fan, X., Zhang, G. and Sun, F., "Effect of Sintering Pressure on the Porosity and the Shear Strength of the Pressure-Assisted Silver Sintering Bonding," In IEEE Transactions on Device and Materials Reliability, vol. **18**, no. 2, (2018) pp. 240-246.

[31] Fu, S., Mei, Y., Li, X., Ning, P. and Lu, G.Q., "Parametric Study on Pressureless Sintering of Nanosilver Paste to Bond Large-Area (≥ 100 mm2) Power Chips at Low Temperatures for Electronic Packaging," Journal of Electronic Materials, vol. **44**, no. 10, (2015) pp. 3973-3984.

[32] Siow, K.S. and Chua, S.T., "Thermal Ageing Studies of Sintered Micron-Silver (Ag) Joint as a Lead-Free Bonding Material," Metals and Materials International, vol. **26**, no. 9, (2020) pp. 1404-1414.
[33] Kuczynski, G.C., "Self-Diffusion in Sintering of Metallic Particles," In Sintering Key Papers, Springer, Dordrecht, (1990) pp. 509-527.
[34] Chen, C., Yeom, J., Choe, C., Liu, G., Gao, Y., Zhang, Z., Zhang, B., Kim, D. and Suganuma, K., "Necking Growth and Mechanical Properties of Sintered Ag Particles with Different Shapes under Air and N2 Atmosphere," Journal of Materials Science, vol. **54**, no. 20, (2019) pp. 13344-13357.
[35] German, R.M., "Sintering Simplified: Surface Area, Density, and Grain Size Relations," In Materials Science Forum, Trans Tech Publications Ltd, vol. **835**, (2016) pp. 50-75.
[36] Yusoff, M. and Hussain, Z., "Effect of Sintering Parameters on Microstructure and Properties of Mechanically Alloyed Copper-Tungsten Carbide Composite," International Journal of Materials, Mechanics and Manufacturing, vol. **1**, no. 3, (2013) pp. 283-286.
[37] Packham, D.E., "Surface Energy, Surface Topography and Adhesion," International Journal of Adhesion and Adhesives, vol. **23**, no. 6, (2003) pp. 437-448.
[38] Cologna, M. and Raj, R., "Surface Diffusion-Controlled Neck Growth Kinetics in Early Stage Sintering of Zirconia, with and without Applied DC Electrical Field," Journal of the American Ceramic Society, vol. **94**, no. 2, (2011), pp. 391-395.
[39] Fang, Z.Z. ed., "Sintering of Advanced Materials," Elsevier, (2010).
[40] Kang, S.J.L., "Sintering: Densification, Grain Growth and Microstructure," Elsevier, (2004).
[41] Siow, K.S., "Die-Attach Materials for High Temperature Applications in Microelectronics Packaging," Materials, Process, Equipment, and Reliability, Springer International Publishing, (2019) pp. 181-196.
[42] Upadhyaya, G.S. Ed., Powder Metallurgy Technology and Equipment: Selected Topics. Trans Tech Publications, (2012).
[43] Wakai, F., Katsura, K., Kanchika, S., Shinoda, Y., Akatsu, T. and Shinagawa, K., "Sintering Force behind the Viscous Sintering of two Particles," Acta Materialia, vol. **109**, (2016) pp. 292-299.
[44] Drioli, E. and Giorno, L., " Basic Aspects of Membrane Science and Engineering," Science Press, (2012).
[45] Chen, C., Noh, S., Zhang, H., Choe, C., Jiu, J., Nagao, S. and Suganuma, K., "Bonding Technology based on Solid Porous Ag for Large Area Chips," Scripta Materialia, vol. **146,** (2018) pp. 123-127.
[46] Salama, H., Kundin, J., Shchyglo, O., Mohles, V., Marquardt, K. and Steinbach, I., "Role of Inclination Dependence of Grain Boundary Energy on the Microstructure Evolution during Grain Growth," Acta Materialia, vol. **188,** (2020) pp. 641-651.
[47] Paknejad, S.A., Dumas, G., West, G., Lewis, G. and Mannan, S.H., "Microstructure Evolution during 300 C Storage of Sintered Ag Nanoparticles on Ag and Au Substrates," Journal of Alloys and Compounds, vol. **617,** (2014) pp. 994-1001.
[48] Li, H., Dey, S. and Castro, R.H., "Kinetics and Thermodynamics of Densification and Grain Growth: Insights from Lanthanum Doped Zirconia," Acta Materialia, vol. **150,** (2018) pp. 394-402.
[49] Osorio, J.D., Maya, D., Barrios, A.C., Lopera, A., Jiménez, F., Meza, J.M., Hernández-Ortiz, J.P. and Toro, A., "Correlations between Microstructure and Mechanical Properties of Air Plasma-Sprayed Thermal Barrier Coatings Exposed to a High Temperature," Journal of the American Ceramic Society, vol. **96,** no. 12, (2013) pp. 3901-3907.

[50] Tsai, J.T. and Lin, S.T., "Silver Powder Effectiveness and Mechanism of Silver Paste on Silicon Solar Cells," Journal of Alloys and Compounds, vol. **548,** (2013) pp. 105-109.
[51] Ordonez-Miranda, J., Hermens, M., Nikitin, I., Kouznetsova, V.G., van der Sluis, O., Ras, M.A., Reparaz, J.S., Wagner, M.R., Sledzinska, M., Gomis-Bresco, J. and Torres, C.S., "Measurement and Modeling of the Effective Thermal Conductivity of Sintered Silver Pastes," International Journal of Thermal Sciences, vol. **108,** (2016) pp. 185-194.